2D Materials

PAPER

Lithographically defined synthesis of transition metal dichalcogenides

Aidar Kemelbay[1,2], Aldiyar Kuntubek[1,2], Nicholas Chang[1,3], Christopher T Chen[1], Christoph Kastl[1], Vassilis J Inglezakis[2], Alexander Tikhonov[2], Adam M Schwartzberg[1], Shaul Aloni[1] and Tevye R Kuykendall[1,4]

1   The Molecular Foundry, Lawrence Berkeley National Laboratory, Berkeley, CA 94720, United States of America
2   Nazarbayev University, Nur-Sultan, 010000, Kazakhstan
3   University of Nevada Las Vegas, 89154-9901 Las Vegas, NV, United States of America
4   Authors to whom any correspondence should be addressed.

E-mail: trkuykendall@lbl.gov and saloni@lbl.gov

Keywords: chalcogenide, TMD, patterning, conversion, lithography

Abstract

Transition metal dichalcogenides (TMDs) promise to revolutionize optoelectronic applications. While monolayer exfoliation and vapor phase growth produce extremely high quality 2D materials, direct fabrication at wafer scale remains a significant challenge. Here, we present a method that we call 'lateral conversion', which enables the synthesis of patterned TMD structures, with control over the thickness down to a few layers, at lithographically predefined locations. In this method, chemical conversion of a metal-oxide film to TMD layers proceeds by diffusion of precursor propagating laterally between silica layers, resulting in structures where delicate chalcogenide films are protected from contamination or oxidation. Lithographically patterned WS_2 structures were synthesized by lateral conversion and analyzed in detail by hyperspectral Raman imaging, scanning electron microscopy and transmission electron microscopy. The rate of conversion was investigated as a function of time, temperature, and thickness of the converted film. In addition, the process was extended to grow patterned MoS_2, WSe_2, $MoSe_2$ structures, and to demonstrate unique WS_2/SiO_2 multilayer structures. We believe this method will be applicable to a variety of additional chalcogenide materials, and enable their incorporation into novel architectures and devices.

Introduction

Nanoscale materials with reduced dimensionality, such as zero-dimensional (0D) nanoparticles, one-dimensional (1D) nanowires, and two-dimensional (2D) layered materials, have been the subject of intense research efforts in recent years due to the many emergent properties that arise at the nanoscale [1]. With the advent of a relatively easy-to-implement exfoliation process for creating one-off devices out of graphene, interest in 2D materials has surged. Transition metal dichalcogenides (TMDs), a family of layered 2D van der Waals materials, have gained interest from the research community thanks to their unique and highly tunable optical and electronic properties [2–4]. There have been considerable efforts to synthesize high-quality TMDs, both for fundamental studies and for integration in next generation devices. Early work [5–7] focused on the preparation of these materials by exfoliation from bulk crystals—similar to those for graphene. While this method is adequate for fundamental studies, it is limited when it comes to large-scale device integration since reproducible patterning and contamination-free fabrication is challenging. To overcome this limitation, a variety of direct-synthesis techniques have been developed—the most prominent among these being chemical vapor deposition (CVD) [8, 9], metalorganic chemical vapor deposition (MOCVD) [10], and atomic layer deposition (ALD) [11]. Some hybrid approaches, such as post-growth annealing of ALD deposited nanocrystalline chalcogenide films [12], or chemical conversion of ALD oxides [13, 14], have also been explored.

There are several key considerations for the successful fabrication and subsequent device integration of TMDs. (1) Controllable synthesis. This involves the growth of materials with high crystallinity, at specific

locations, and of desired thickness. (2) Material properties tuning. Tuning TMD properties can be accomplished by adjusting the structure itself, either *in situ* or post-growth (e.g. varying number of layers, intercalation, and doping) or by designing its environment [15–19]. (3) Integration of TMDs into devices while preserving their desired properties. Once TMDs with the desired properties have been produced, it is important to preserve their properties when exposing them to environmental conditions and to the fabrication processes required for integration into devices. The former is especially important for TMDs with poor air stability [20], while contamination and defects creation throughout the device fabrication process are concerns for all 2D materials. For example, lithographic processing can leave residues on the sensitive TMD surface [21], and passivation of TMDs with dielectrics or other materials, which is required for numerous applications, can lead to oxidation and/or creation of defects [22, 23]. Passivation of TMDs is a challenging process due to the inertness of the basal plane of TMDs, hindering chemical and physical vapor deposition of uniform capping layers [24, 25]. It follows that demonstration of a controllable, site-specific synthesis of TMDs, with pre-programmed structure and materials properties, in an isolated environment would be of major scientific and practical interest.

This work demonstrates a novel synthetic method that enables the fabrication of 2D TMDs with lithographically-predefined structures, and thickness control with few-layer precision. The structures are uniform across greater than centimeter scale and can grow to lateral depths exceeding 100 μm using techniques amenable to wafer-scale processing. The 2D material is grown as a buried layer—encapsulated by SiO_2 without further processing steps—providing a platform for contamination-free integration into devices. The synthesis is achieved by first encapsulating an ALD grown metal oxide (MO_x) film between SiO_2 layers, then patterning and etching to expose the edges of the metal oxide. The buried MO_x film is subsequently chemically converted into a metal chalcogenide, laterally from the exposed edges. The approach promotes lateral (in-plane) growth of TMDs, in a process we term 'lateral conversion'. The method is distinct from widely used MOCVD, CVD, and ALD methods in which films are directly deposited—or grown on a substrate, and is also distinct from conversion of exposed ALD oxide films to chalcogenides [13, 14, 26–28]. The presented lateral conversion methodology and the properties of the resulting materials were studied in detail for the conversion of WO_x to WS_2. The films were characterized by a variety of analytical techniques, including x-ray photoelectron spectroscopy (XPS), hyperspectral Raman imaging, scanning electron microscopy (SEM), and transmission electron microscopy (TEM). To show the effectiveness and generalizability of this technique, the process was extended to demonstrate the growth of WSe_2, MoS_2, and $MoSe_2$, and we believe

it will be applicable to other relevant chalcogenides. To demonstrate one of the unique capabilities of this method, we fabricated stacked multilayer structures composed of repeating SiO_2/WS_2 units. We believe this unique lateral conversion methodology will further enable a variety of other unique advanced architectures, such as complex (3D) nanophotonic structures [29, 30].

Results and discussion

The fabrication of lithographically patterned TMD structures via lateral conversion is achieved by a several-step process, which is illustrated in the cross-sectional schematic presented in figure 1(a). First, a multilayer film is deposited: a metal-oxide (MO_x) thin-film is deposited on a Si/SiO_2 thermal oxide substrate by plasma enhanced ALD. ALD allows angstrom-level precision of the layer thickness and can be varied to achieve the desired number of TMD layers, as will be shown later. To create a buried layer for lateral conversion and to ensure the preservation of a clean, high-quality interface between the SiO_2 and the metal-oxide, the MO_x film is subsequently covered with a few nanometers of SiO_2 by ALD. Additional SiO_2 is deposited by plasma enhanced chemical vapor deposition (PECVD) to increase the barrier layer thickness while reducing total deposition time. The substrate is then patterned using standard photolithography techniques, and dry etched with CHF_3 + Ar, resulting in the structure depicted in figure 1(a)(left). The photoresist is removed and the samples are transferred to a tube furnace reactor. The process of chemical conversion of the MO_x layer into MX_2 is carried out in two steps. First, the sample is annealed in an Ar/H_2 gas mixture, reducing the MO_x layer to metal, as depicted in figure 1(a)(center). Next, it is chalcogenated by exposure H_2X to form the TMD (MX_2). The resulting structure is depicted in figure 1(a)(right).

The process outlined above was used to convert WO_3 to WS_2. True-color white light reflectance microscope (WLRM) images, showing substrates at key steps in the process, are presented in figure 1(b). The difference in color in the images is due to changes in thickness and index of refraction of the films as their composition changes. Figure 1(b)(left), shows an as-made patterned substrate with 4.8 nm of WO_3 deposited on 250 nm SiO_2 thermal-oxide on silicon, and coated with ~55 nm of SiO_2. The WO_3/SiO_2 layers appear light blue, with the etched regions (~100 nm deep) appearing white. After reduction in an Ar/H_2 gas mixture at 750 °C, the tungsten layer is composed primarily of metallic tungsten, and appears purple, as shown in figure 1(b)(center). The layer was then sulfidized by introducing H_2S into the Ar/H_2 mixture at 750 °C, resulting in formation of WS_2 encapsulated by SiO_2. To visually observe the difference between converted and unconverted regions, the sulfidation
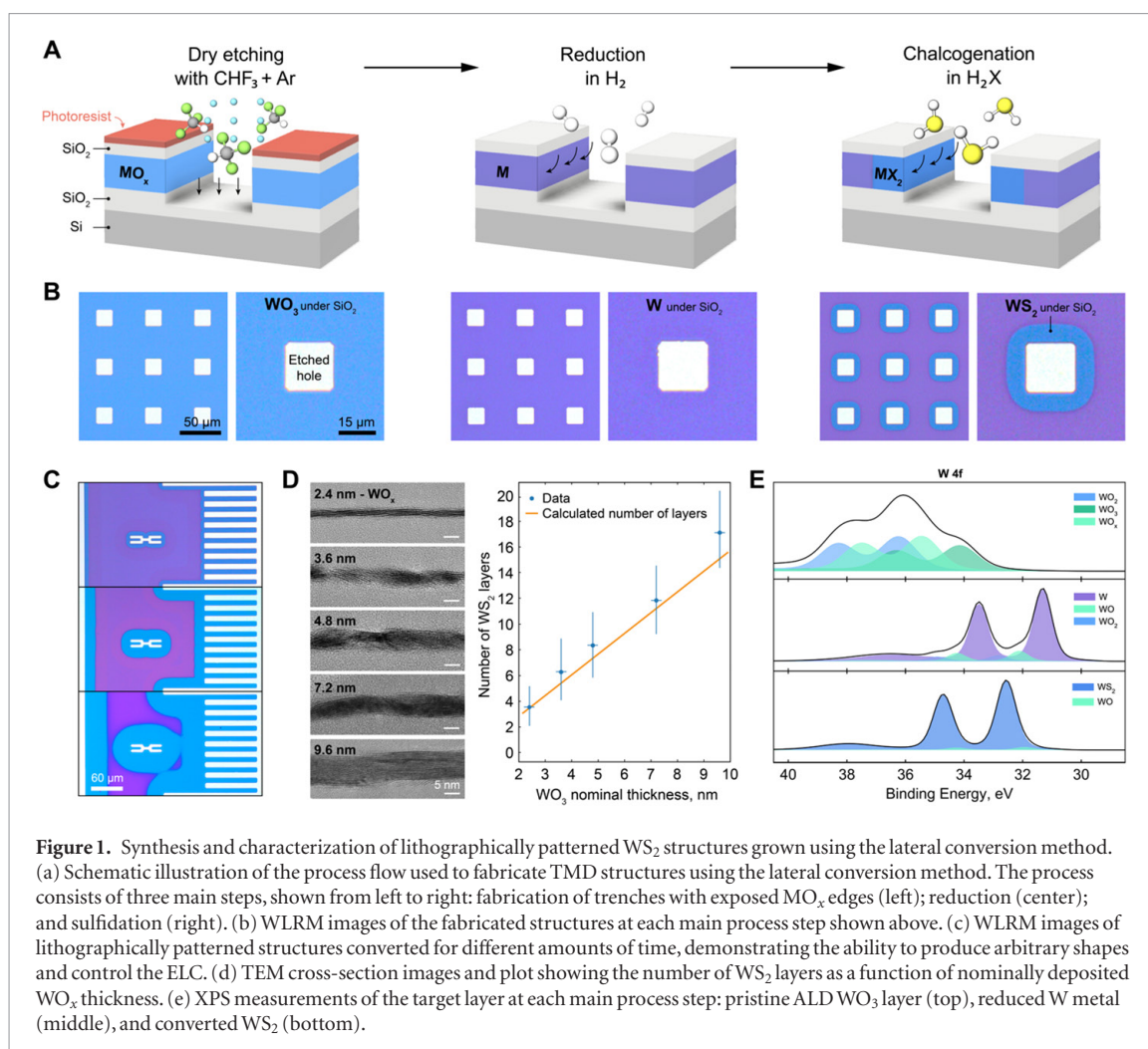
Figure 1. Synthesis and characterization of lithographically patterned WS$_2$ structures grown using the lateral conversion method. (a) Schematic illustration of the process flow used to fabricate TMD structures using the lateral conversion method. The process consists of three main steps, shown from left to right: fabrication of trenches with exposed MO$_x$ edges (left); reduction (center); and sulfidation (right). (b) WLRM images of the fabricated structures at each main process step shown above. (c) WLRM images of lithographically patterned structures converted for different amounts of time, demonstrating the ability to produce arbitrary shapes and control the ELC. (d) TEM cross-section images and plot showing the number of WS$_2$ layers as a function of nominally deposited WO$_x$ thickness. (e) XPS measurements of the target layer at each main process step: pristine ALD WO$_3$ layer (top), reduced W metal (middle), and converted WS$_2$ (bottom).

step was intentionally stopped before converting the entire film. In figure 1(b)(right), converted regions are observed only around etched holes, with WS$_2$ appearing dark blue. This basic demonstration of the process shows that the conversion proceeds laterally from the lithographically patterned edges and demonstrates the effectiveness of the SiO$_2$ capping layer in preventing penetration of sulfide into the reduced metallic layer from the top. Figure 1(c) shows three structures that were lithographically patterned and converted to WS$_2$ with increasing time or temperature (from top to bottom). These are arbitrarily patterned 'test structures', used to demonstrate the type of patterning that can be achieved with this method. It shows the conformal nature of the growth front, demonstrating that the extent of lateral conversion (ELC) can be controlled to create ribbon-like structures around the edges of a pattern when shorter conversion times are used, or to fully convert arbitrary shapes, filling areas when longer conversion times are used.

To test our ability to control the thickness of the TMD layers, samples with 2.4, 3.6, 4.8, 7.2 and 9.6 nm thick WO$_x$ films were fabricated, corresponding to desired WS$_2$ films with 3, 5, 8, 11 and 15 layers, respectively. The samples were converted using the process parameters described above. Figure 1(d)(left) shows representative high-resolution TEM cross-sectional

images of the WS$_2$ layers, labeled with the corresponding deposited WO$_x$ film thickness. For simplicity, going forward we will refer to samples using their initial ALD oxide thicknesses. The cross-sections show highly-oriented WS$_2$ films with programmable thickness control, and a measured interlayer spacing of ~6.2 Å, which closely matches the lattice spacing in the *c*-direction of pristine WS$_2$. The average number of WS$_2$ layers in the film were counted at 30 locations along the 10 μm cross-sections, and summarized in figure 1(d)(right). The error bars describe the span of the thickness values (maximum and minimum number of layers counted), which shows excellent agreement to the expected number of layers (demarcated by the orange line) that were calculated based on the nominal thickness of the WO$_x$ layer. Additional TEM results and analysis are presented later.

XPS was used to follow the chemical changes at each stage of the conversion process (figure 1(e). Since the target layer is buried beneath SiO$_2$, depth-resolved spectra were acquired by controllably sputtering the sample. The spectral shift of the W4f$_{7/2}$ peak, often referred to as chemical shift, is a clear signature of W oxidation state. The peak appears at binding energies of 31.3 eV for W metal, at 32.4 eV for WS$_2$, and at 33.6 eV and 36.1 eV for WO$_2$ and WO$_3$, respectively. Spectra were analyzed to reveal the chemical state by fitting

with a minimal number (2–3) of components, each composed of a W4f doublet and a broad W5s feature at higher binding energy. The spectrum of the ALD tungsten oxide precursor is indicative of a complex oxide, requiring at least three oxide-like components including WO_2, WO_3, and one with an intermediate oxidation state. Complex oxide-character is often seen in ALD oxide films and has been reported for ALD tungsten oxide [31]. The W4f feature changes drastically as a result of the reduction step and becomes almost exclusively metallic in character, with less than 8% residual oxide components. Following sulfidation, the W4f signature is almost exclusively of WS_2 in character, with less than 2% residual WO_x-like species.
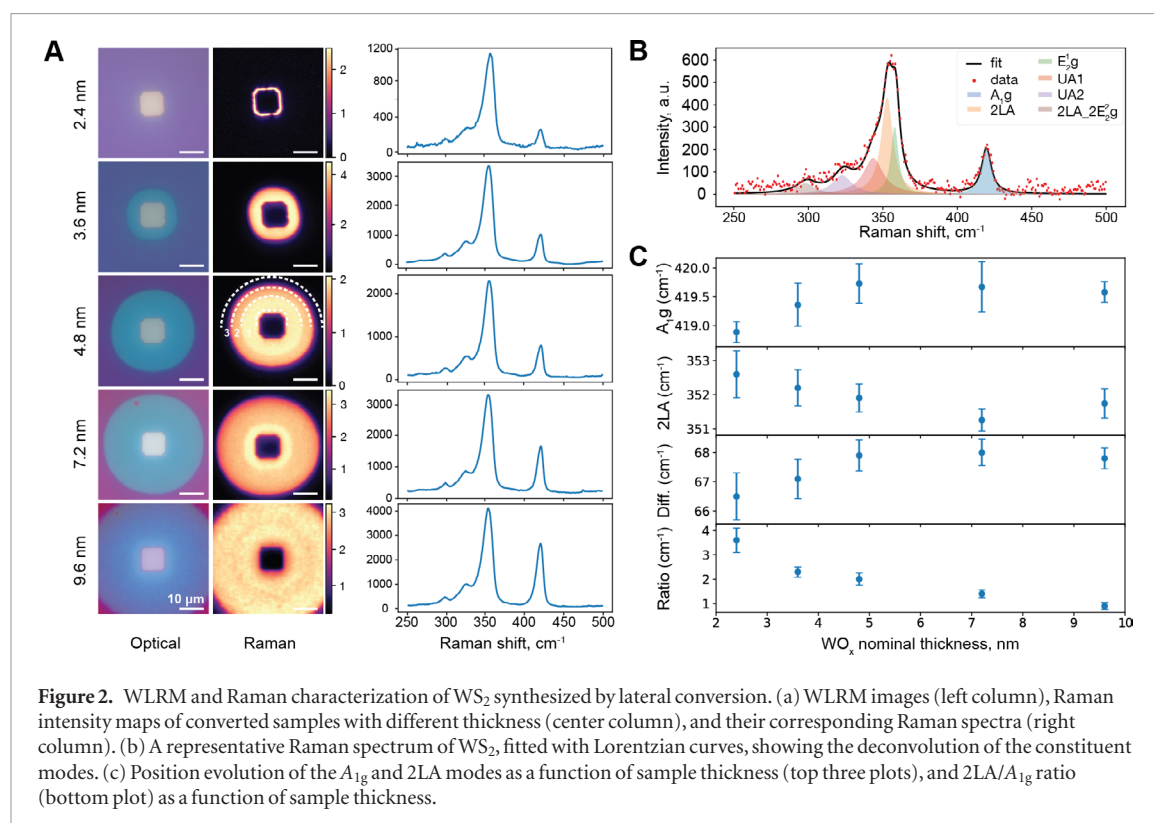
While the changes in color observed by WLRM images appear to provide a good estimate of the ELC, additional spectroscopic methods are needed to study the properties of the converted layer in more detail. Raman spectroscopy of WS_2 can allow us to extract the film's quality, orientation, and thickness [32]. WLRM images and Raman spectra, presented in figure 2, were collected for five samples with increasing WO_x thickness, which were converted to WS_2 using identical conditions. WLRM images are shown in Figure 2(a)(left column). The corresponding confocal micro-Raman images shown in figure 2(a)(center column), map the integrated intensity of the WS_2 spectral component, which was extracted from the hyperspectral image data collected for each sample. The average Raman spectra are shown figure 1(a)(right column). In the three thickest samples, 3 regions are demarcated on the center Raman map by a white dashed line. The intensity of the Raman signal is highest in region 1 near the exposed edge. This is followed by a significant decrease in uniformity and intensity of the Raman signal from region 1 to region 2, indicating that the quality and uniformity of the WS_2 film is decreased in this region. The intensity of the Raman signal then drops off abruptly at the interface between region 2 and the unconverted metal layer in region 3. These observations are consistent with a diffusion driven mechanism for the conversion process: complete conversion to sulfide near the exposed film edge, a two-phase region—where residual unreacted tungsten and WS_2 are present together, and an abrupt conversion endpoint that is defined by the diffusivity of the sulfur in the buried layer.

Analysis of Raman spectral features can be used to extract information about the WS_2 thickness. It has been shown that as the thickness of exfoliated WS_2 sample decreases, the intensity ratio of the 2LA to A_{1g} mode increases, while the separation between the two modes decreases [33]. Due to significant overlap between spectral components of WS_2 Raman signature, the spectrum must be fit with a set of Lorentzian functions for the intensity of the 2LA mode to be accurately extracted (figure 2(b)). Each spectrum in the Raman hyperspectral image has been individually fitted. The relevant values have been extracted and plotted against the nominal WO_x thickness (fig-

ure 2(c)). The intensity ratio of the 2LA/A_{1g} modes increases with decreasing sample thickness, mostly as a result of the decline of the A_{1g} mode intensity; also, the 2LA mode position is red shifting, while the A_{1g} mode is blue shifting at the same time. These trends are almost identical to the ones referenced above [33], and can be interpreted as microscopic confirmation of the thickness and structure of the films. The Raman results confirm that the thickness of the WS_2 layer is defined by that of the original WO_x layer, and also show that we can interpret the color contrast in WLRM images to measure the ELC. These are valuable feedback parameters for the study of the kinetics and thermodynamic mechanisms of this process.

While Raman spectroscopy is a good indicator of general material quality, atomically-resolved imaging by TEM can help us better understand the morphology, microstructure, and conversion mechanisms. Figure 3(a) shows a WLRM image (left), confocal Raman map (center), and an SEM image (right). The WLRM image and Raman map show variations in color and intensity, consistent with those discussed above, and were used to select the specific sites from which TEM cross sections were extracted. The exposed edge is on the left-hand side, with conversion proceeding from left to right. The boxes drawn on the SEM image indicate the regions from which two, ~14 μm long, 10–50 nm thick TEM cross-sections were extracted by focused ion beam (FIB) milling [34] (labeled 'FIB 1' and 'FIB 2'). Panoramic TEM images of the cross-sections are shown in figures 3(b) and (c) (top). A series of six high-resolution TEM (HRTEM) images, allowing detailed structural characterization, were taken at regular intervals—roughly corresponding to their positions below the panoramic image. In figure 3(b), the HRTEM images reveal a highly-oriented continuous WS_2 film near the exposed edge on the left-hand side of region 1. This region is correlated with the highest intensity area seen in Raman map in figure 3(a). Proceeding to the right, into region 2, the WS_2 layers show more disorder, and occasionally small grains of unconverted W are observed. Modulations in layer numbers and evidence of gaps between grains are also seen. These modulations explain the intensity variations observed in the Raman images. In figure 3(c), as we approach the end of the converted region, midway through region 3, the film is almost exclusively composed of pure W metal, with small amounts of WS_2 visible at the grain boundaries between the W domains. These observations are consistent with a diffusion mechanism paired with chemical reactions that immobilize sulfur as it is incorporated into WS_2. The presence of small amounts of WS_2 past zone 3, at the grain boundaries of the W film, indicates the importance of grain boundary diffusion in the conversion process.

Figure 3(d) shows a cross-sectional HRTEM image of the thinnest sample studied, synthesized by lateral conversion of a 2.4 nm thick WO_3 film. The resulting

Figure 2. WLRM and Raman characterization of WS_2 synthesized by lateral conversion. (a) WLRM images (left column), Raman intensity maps of converted samples with different thickness (center column), and their corresponding Raman spectra (right column). (b) A representative Raman spectrum of WS_2, fitted with Lorentzian curves, showing the deconvolution of the constituent modes. (c) Position evolution of the A_{1g} and 2LA modes as a function of sample thickness (top three plots), and 2LA/A_{1g} ratio (bottom plot) as a function of sample thickness.

WS_2 is highly crystalline and consists of 4 ± 1 layers showing a high degree of in-plane alignment. No mixed WS_2/W or unconverted regions were observed along the entire cross-section, and the WS_2 film was observed to terminate abruptly at the transition to W. Such precise control over the number of layers and the ability to grow WS_2 on micron scale, together with lithographic compatibility and pre-existing protection layer makes this material a promising candidate for few-layer electronic and optoelectronic devices. Further scale down of the precursor oxide and conversion process optimization may lead to (near-) monolayer material.

To gain mechanistic understanding of the factors governing the kinetic and thermodynamic aspects of the lateral conversion process, we measured the ELC as a function of sample thickness, temperature, and reaction time. Other parameters, such as gas flow rates, pressure, and temperature ramp rates were kept constant. Two methods were used to evaluate the ELC: (1) Raman line profiles were acquired perpendicular to the exposed edge using a Horiba confocal microscope, and (2) color changes were observed by WLRM and measured. From the Raman line profile, the integrated intensity of the A_{1g} and the $2LA + E_{2g}^1$ peaks were extracted. Figure 4(a) shows a plot of intensity as a function of distance (top) and the corresponding WLRM image (bottom) for a laterally converted sample. Raman line scans and WLRM color changes were observed to be correlated in a large number of samples, thus we determined that WLRM can be used as a fast and accurate proxy measurement to determine the ELC. The ELC shown for the following studies were

measured by programmatically extracting the intensity profiles from WLRM images based on color differences between the converted and unconverted regions.

To study the kinetics of the conversion process, we reduced the samples in Ar/H_2 atmosphere at 750 °C for 120–180 min to ensure full reduction of the WO_x layer. Subsequently, samples of varying thicknesses were sulfidized for times varying from 15 to 120 min. The measured ELC values are shown in figure 4(b). For the thinnest samples the ELC is smaller than 1.4 μm and too close to the optical microscopy resolution to establish accurate time dependence. For all other samples, the ELC increases with increasing sulfidization time. The ELC for the 3.6 nm samples is somewhat flat, but shows an increase for long conversion times. The ELC for the 4.8 nm samples increase linearly with time, while the two thickest samples show a steep increase after 60 min.

Figure 4(c) shows the temperature-dependent conversion experiments. Samples were annealed in H_2 at 750 °C, then sulfidized at temperatures ranging between 650 and 800 °C for 30 min. Similar to the time-dependent experiments, the ELC for the thinnest samples (<2 μm) are on the order of the optical microscopy resolution limit, making the temperature dependence of the 2.4 nm thick sample hard to measure. For all other thicker samples, the trend generally shows that increasing reaction temperature results in a larger ELC. However, they do not follow the expected Arrhenius behavior, suggesting that the kinetics are more complex than a single path random walk diffusion. The trend breaks down beyond 800 °C, with samples showing erratic ELC. We suspect this is
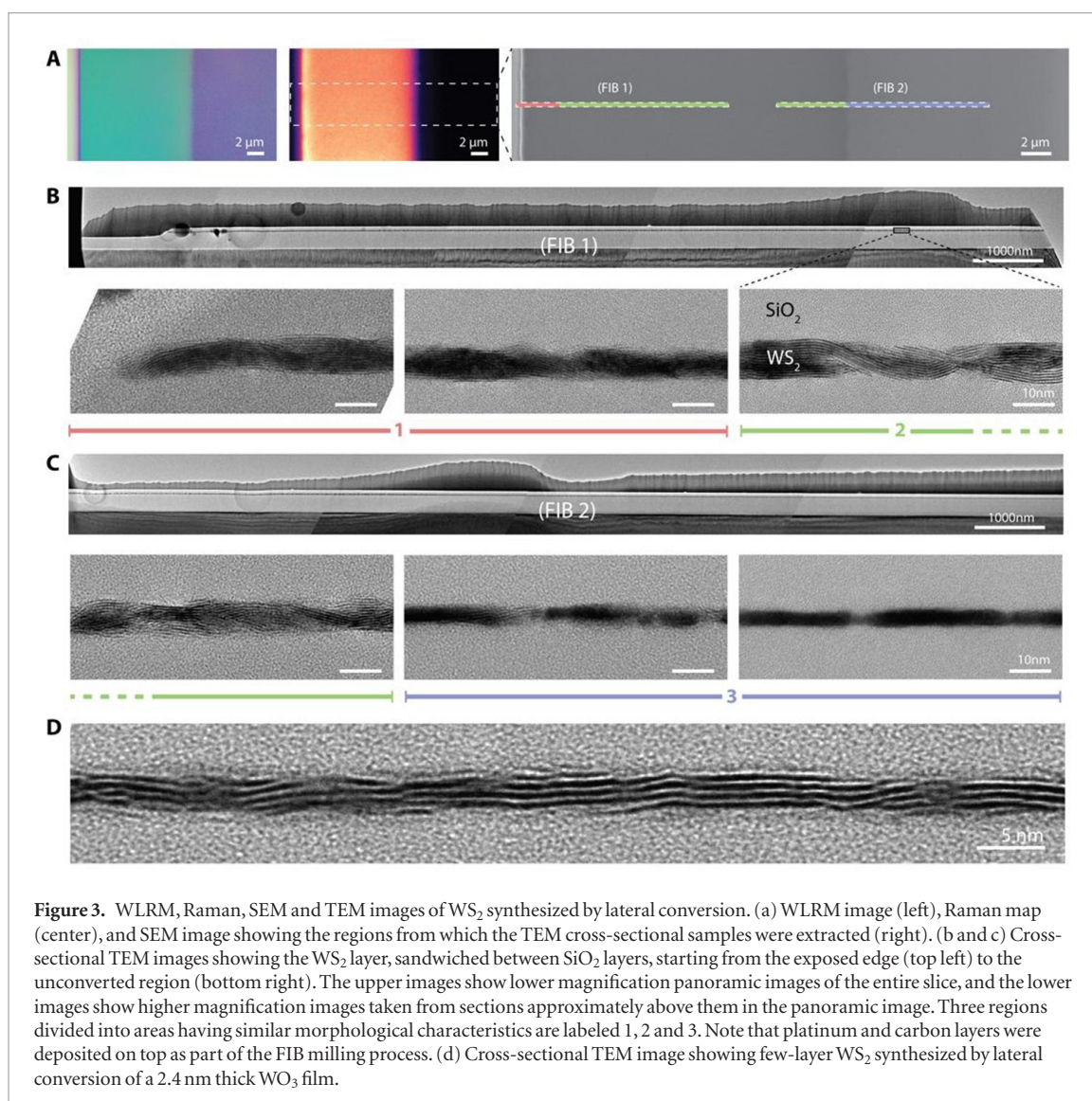
Figure 3. WLRM, Raman, SEM and TEM images of WS$_2$ synthesized by lateral conversion. (a) WLRM image (left), Raman map (center), and SEM image showing the regions from which the TEM cross-sectional samples were extracted (right). (b and c) Cross-sectional TEM images showing the WS$_2$ layer, sandwiched between SiO$_2$ layers, starting from the exposed edge (top left) to the unconverted region (bottom right). The upper images show lower magnification panoramic images of the entire slice, and the lower images show higher magnification images taken from sections approximately above them in the panoramic image. Three regions divided into areas having similar morphological characteristics are labeled 1, 2 and 3. Note that platinum and carbon layers were deposited on top as part of the FIB milling process. (d) Cross-sectional TEM image showing few-layer WS$_2$ synthesized by lateral conversion of a 2.4 nm thick WO$_3$ film.

due to the formation of silicon disulfide from around the edges of the substrate where the silica passivation layer is thinnest. A related observation is that samples containing small cracks or scratches (exposing Si to H$_2$S) are prone to formation of silicon disulfide. The observation of SiS$_2$ formation seemed to correlate with inconsistent WS$_2$ growth. We performed experiments on quartz substrates, which showed similar time and temperature dependence, but were able to withstand higher temperatures, supporting premise that Si plays a role.

Though the time/temperature dependent conversion rates do not seem to follow a simple diffusion-rate mechanism, we speculate that there are three mechanisms for the diffusion of H$_2$S through the film that occur simultaneously, each with different rates. (1) Diffusion through the relatively large space between van der Waals bonded layers, (2) grain boundary diffusion through W and WS$_2$, and (3) diffusion through voids inside W or WS$_2$, which were formed as a result of volume shrinkage during the reduction of WO$_3$ to W metal. Each of these likely contribute to the complex non-Arrhenius diffusion behavior observed.

The reduction step plays an important role in the lateral conversion process. Interestingly, when H$_2$S or H$_2$S/H$_2$ gas mixture was used without a separate reduction step, very little conversion was observed. The small amount of conversion that was observed, generally did not penetrate very deeply into the film or was very non-uniform. To assess the impact of the reduction step, samples were reduced in H$_2$—varying the reduction time from 15–60 min while holding the subsequent sulfidation time constant at 120 min. The results presented in figure 4(d) show that the ELC increases with increasing reduction time. This suggests that: (a) the reduction of WO$_x$ to W metal also proceeds laterally, (b) that the reduction step is crucial for uniform lateral conversion to WS$_2$, and (c) that the ELC is limited by the extent of reduction. It is worth noting that direct deposition and lateral conversion of metallic W, without the requirement for a reduction step, may also be interesting to study, however, the method we demonstrate has several significant benefits. ALD provides uniform, angstrom-level thickness-control over large areas and allows the ability to coat high aspect ratio structures—potentially enabling
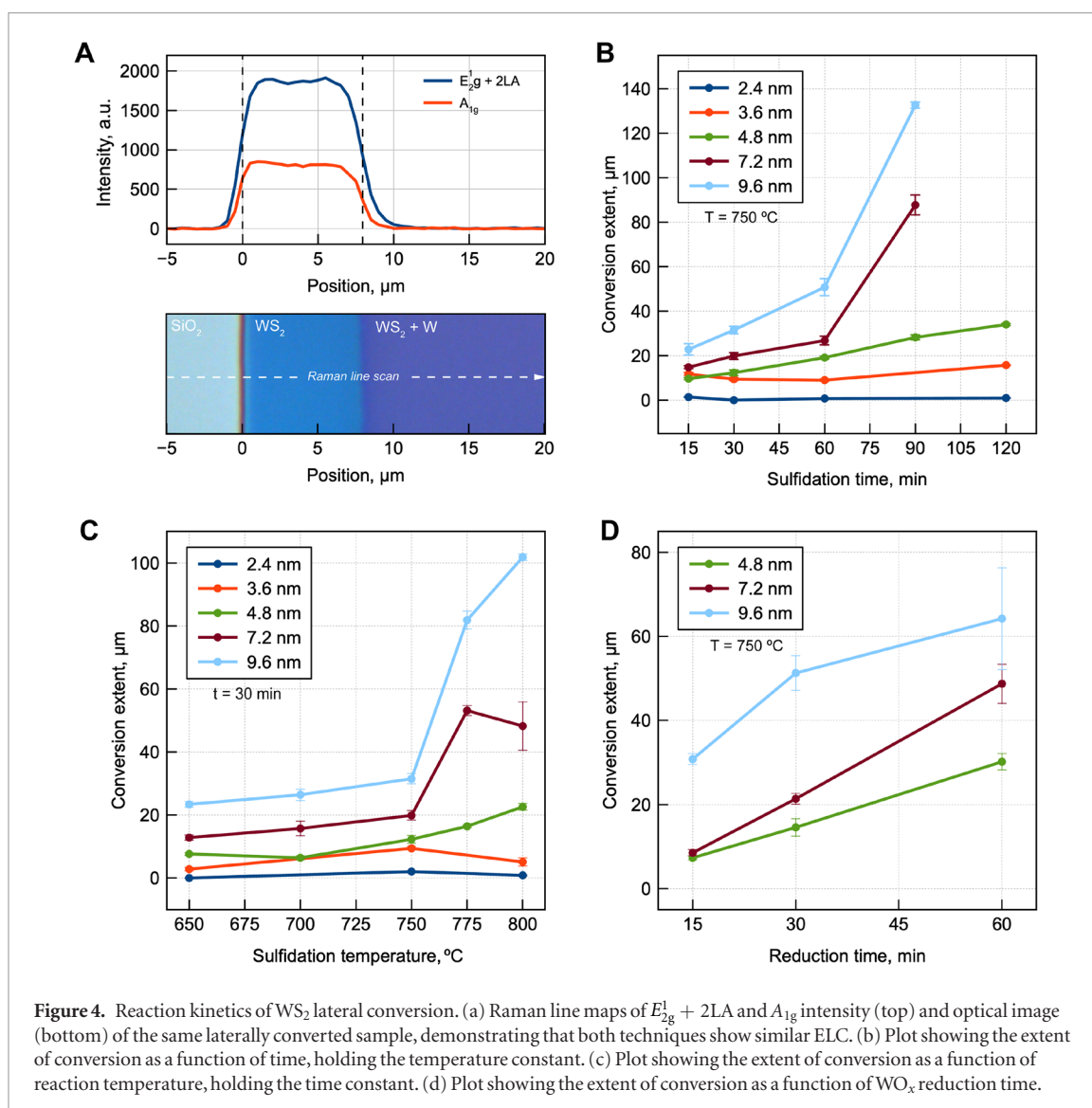
Figure 4. Reaction kinetics of WS$_2$ lateral conversion. (a) Raman line maps of E_{2g}^1 + 2LA and A_{1g} intensity (top) and optical image (bottom) of the same laterally converted sample, demonstrating that both techniques show similar ELC. (b) Plot showing the extent of conversion as a function of time, holding the temperature constant. (c) Plot showing the extent of conversion as a function of reaction temperature, holding the time constant. (d) Plot showing the extent of conversion as a function of WO$_x$ reduction time.
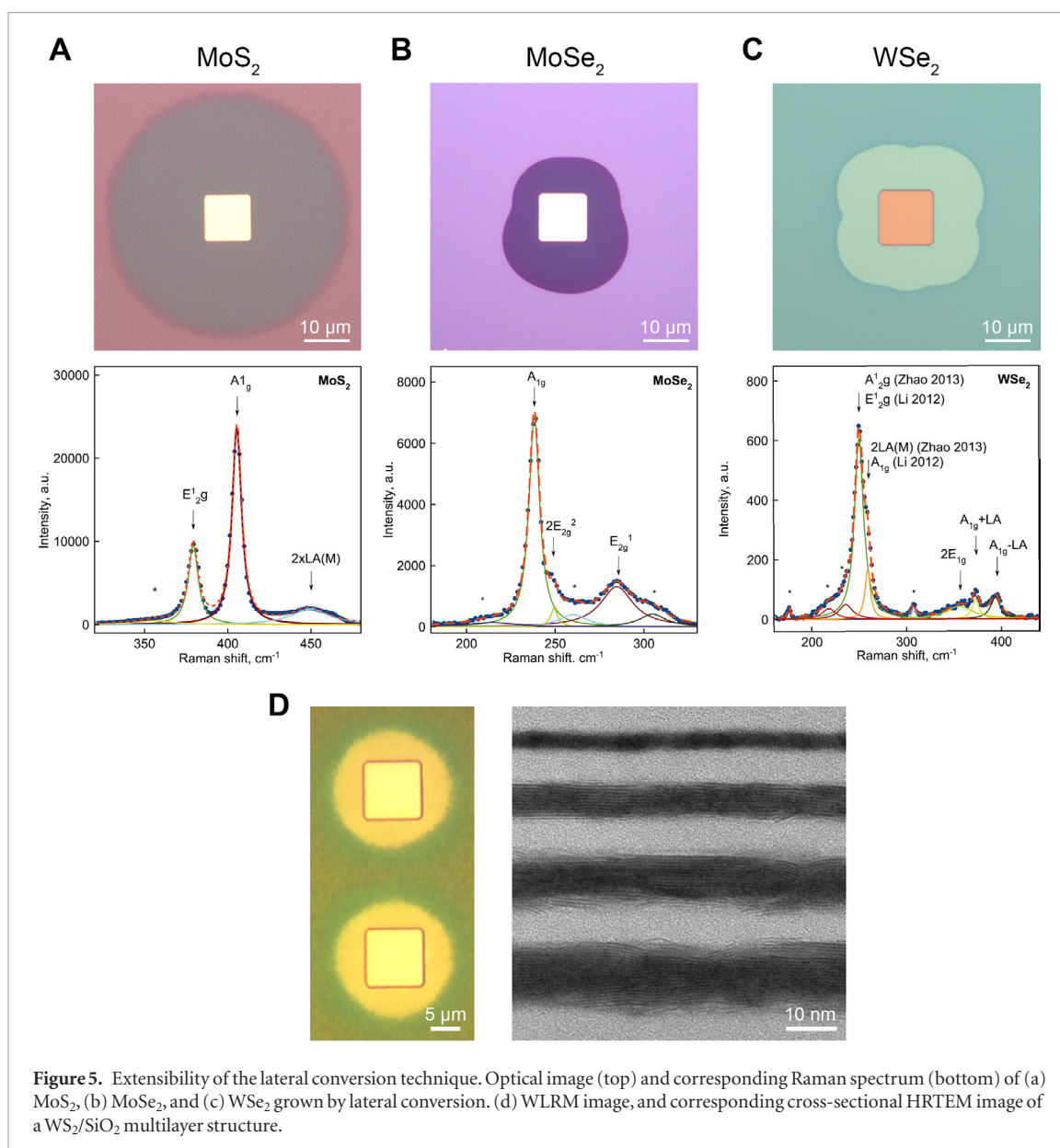
more diverse 3D architectures and applications of TMDs created using this method. Additionally, metal films below ~5 nm are difficult to achieve without significant island formation, which would likely result in discontinuous and inconsistent TMD films.

In addition to WS$_2$, we were able to extend our lateral conversion technique to fabricate MoS$_2$, WSe$_2$, MoSe$_2$, and a stacked multilayer structure. Figure 5 shows optical images and corresponding Raman spectra for these TMDs. Raman modes were assigned based on those observed in previous work [35–38], and confirm the composition of the films. While the conversion extent of the WSe$_2$ and MoSe$_2$ materials do not demonstrate the near-perfect contour that we observe for WS$_2$ and MoS$_2$, we believe it can be improved with some process optimization, and it suggests that the lateral conversion method should be generalizable to the growth of other TMDs. In figure 5(d), a stacked multilayer structure is shown, consisting of four WO$_x$ layers with different thickness—separated by SiO$_2$—laterally converted to WS$_2$. A WLRM image of the multilayer structure with three distinct colors around etched holes is shown (left), and a TEM cross-section of the

same structure is shown (right). Due to the thickness differences between the WO$_x$ layers, the ELC are different for each layer, resulting in the multi-colored concentric rings that were observed by WLRM. TEM measurements show well-aligned, alternating layers of WS$_2$ and amorphous SiO$_2$. The topmost layer, however, consists of metallic W and does not show conversion. This is also evidenced by the display of only three colors in the WLRM image as opposed to the expected four colors. We suspect that the layer failed to convert due to redeposition of SiO$_2$ during RIE, obstructing the opening through which chalcogen diffusion should occur. Optimization of this process is required, nonetheless, we think this is a significant result, showing a unique capability and flexibility of this approach.

Conclusion

In conclusion, we demonstrate the growth of TMD materials by lateral conversion of metal-oxide layers encapsulated between SiO$_2$ layers. The approach enables the formation of precisely patterned TMD structures using standard lithographic techniques

Figure 5. Extensibility of the lateral conversion technique. Optical image (top) and corresponding Raman spectrum (bottom) of (a) MoS_2, (b) $MoSe_2$, and (c) WSe_2 grown by lateral conversion. (d) WLRM image, and corresponding cross-sectional HRTEM image of a WS_2/SiO_2 multilayer structure.

and tools widely used in industry and academia, such as ALD and dry etching. The converted materials were analyzed using WLRM, Raman spectroscopy, XPS, and TEM. Raman measurements were able to clearly identify the TMDs, and provided evidence for the reduction in number of WS_2 layers with reduced initial WO_x thickness. Cross-sectional TEM images of the laterally converted films revealed the morphology, microstructure, conversion mechanisms, and few-layer thickness control of the WS_2 layer. Kinetic and thermodynamic aspects of the lateral conversion mechanism were studied, exploring changes in conversion rate as a function of film thickness.

Looking forward, we believe that layer control and crystallinity of the materials can be further optimized. Synthesis of TMDs encapsulated between SiO_2 or other protective layers should act to preserve the as-grown material quality without degrading its properties or contaminating it during subsequent processing steps, thus providing a way to grow and improve the long-term stability of oxidation-prone materials. This method can likely be extended to be used with other technologically useful encapsulating dielectric materials or epitaxial substrates, such as h-BN, graphene, other high-k dielectrics, sapphire, etc. Because ALD allows conformal coating of complicated and high-aspect ratio structures, this method could also enable integration of TMDs into 3D architectures. Finally, different metals and chalcogens could be used to synthesize a large variety of different TMD materials and TMD vertical or lateral heterostructures.

Methods

Fabrication and conversion

Metal oxide (MO_x) thin-film, between 2–10 nm was deposited on a Si wafer with 250 nm thermal oxide in an Oxford FlexAl ALD at 300 °C. An oxygen plasma was used as the oxygen source. The tungsten precursor was bis(tert-butylimino) bis(dimethylamino)tungsten(VI). The molybdenum precursor was molybdenum hexacarbonyl. Our

process demonstrated linear cycle-to-thickness growth dependence with WO_3 and MoO_3 deposition rates of 0.5 Å/cycle and 0.7 Å/cycle respectively. The film thickness was confirmed using an *in situ* Woolam M-2000 ellipsometer. The MO_x film was subsequently covered with 4.3 nm of SiO_2 by ALD without breaking the vacuum, using tris(dimethylamino)silane and oxygen plasma. Substrates were transferred to an Oxford 80 + PECVD to grow an additional 50 nm of SiO_2, using 1% SiH_4 in Ar and N_2O (1182 sccm and 710 sccm, 350 °C, 10 W). Various test-patterns were created on the substrate using ma-N 1420 negative tone photoresist, and standard photolithography techniques. The samples were dry etched with $Ar + CHF_3$ (25 sccm + 35 sccm, 100 W, 30 mTorr) in an Oxford 80 + Reactive Ion Etching system to a depth of about 100 nm. After etching, the photoresist mask was removed in hot acetone and samples were annealed for 10 min in O_2 plasma (50 sccm, 150 W, 100 mTorr) to remove photoresist residues and the polymer layer known to form on trench sidewalls during dry etching. Larger wafers were then cleaved into smaller samples for conversion. To prevent the chalcogen precursor from attacking the exposed silicon on the edges of the substrates during the conversion step, the edges of the substrates were placed face-down and coated with 50 nm of SiO_2 in the PECVD system. Next, the substrates were transferred to a MTI Crystal 1200x-RTP-4 tube furnace reactor for conversion. To reduce the MO_x film, the samples were heated to between 650 °C–750 °C in 40 s, in 1000 sccm Ar and 50 sccm H_2 at atmospheric pressure, and held for up to 2 h. The metal was then chalcogenated by introducing 25 sccm of H_2S into the Ar/H_2 mixture at between 650 °C–850 °C at a pressure of 100 torr. To ensure accurate conversion times, rapid gas exchange was achieved by quickly pumping to base pressure and refilling with the desired $Ar/H_2/H_2S$ mixture. At the end of the reaction time, the system was again pumped to base pressure and refilled with Ar and allowed to cool. The selenide samples were prepared using a similar procedure, in a Lindberg Blue HTF55322C tube furnace, a 1″ quartz tube, 500 sccm Ar, 25 sccm H_2, and 12.5 sccm H_2Se at 760 torr. Annealed temperature of 750 °C, and conversion temperature of 650 °C.

Optical characterization
WLRM images were obtained using a Leica DM2500-M microscope.

Raman spectroscopy maps were performed on a custom Raman microscope built on a Nikon Eclipse Ti inverted microscope. The sample was illuminated with a 532 nm laser which was focused to a diffraction limited spot with a Nikon 100 × 0.95 NA objective. The sample was rastered with a MadCityLabs Piezo scan stage. Spectra were recorded with an Acton 2300i spectrometer with an 1800 grooves mm^{-1} grating and a Princeton Instruments PIXIS CCD. The sample is scanned over an area up to 49 μm^2. Data acquisition

is performed using Scope Foundry Software [39] and processed using Python's matplotlib [40], scipy [41] and hyperspy [42] libraries. Raman maps represent integrated intensities of the WS_2 signal component extracted by means of principal component analysis using non-negative matrix factorization algorithm [43].

Raman line scans and point spectra were also obtained on Horiba Jobin Yvon LabRAM ARAMIS confocal microscope, with 532 nm Nd:YAG laser, focused by a 100× objective of 0.9 numerical aperture and the spectra were processed using the LabSpec 6 software.

X-ray photoelectron spectroscopy
XPS measurements were performed using Thermo Scientific K-Alpha x-ray photoelectron spectrometer system, using a monochromatic Al Kα x-ray ($hv = 1486.7$ eV), equipped with an ion gun for depth profiling. The latter was operated in a monatomic mode at 1 keV, with typical sputtering rates of SiO_2 of 5 nm min^{-1}.

Electron microscopy
SEM measurements were performed using Zeiss Ultra 55 SEM at an accelerating voltage of 5 kV. Cross-sectional samples were milled using a FEI Helios G4 UX dual beam focused ion beam (FIB). The sample surface was first protected using electron beam induced deposition of carbon and platinum followed by additional platinum layer deposition using and ion beam. Next a sample was millled-out using a standard procedure common for thin film sample preparation. The sample was mounted on a Copper grid and thinned to 10-50 nm thickness. TEM imaging was performed using a JEOL 2100F TEM, at an accelerating voltage of 200 kV. The image contrast and brightness were adjusted in Gatan Digital Micrograph 3.0.

Acknowledgment

ORCID iDs

Aidar Kemelbay ⓘ https://orcid.org/0000-0002-3321-1483
Christopher T Chen ⓘ https://orcid.org/0000-0001-5848-961X
Christoph Kastl ⓘ https://orcid.org/0000-0001-5309-618X

Vassilis J Inglezakis https://orcid.org/0000-0002-0195-0417

Alexander Tikhonov https://orcid.org/0000-0001-6302-6599

Adam M Schwartzberg https://orcid.org/0000-0001-6335-0719

Shaul Aloni https://orcid.org/0000-0002-7561-4336

Tevye R Kuykendall https://orcid.org/0000-0003-1362-3285

References

[1] Chhowalla M, Shin H S, Eda G, Li L-J, Loh K P and Zhang H 2013 The chemistry of two-dimensional layered transition metal dichalcogenide nanosheets *Nat. Chem.* **5** 263–75

[2] Radisavljevic B, Radenovic A, Brivio J, Giacometti V and Kis A 2011 Single-layer MoS$_2$ transistors *Nat. Nanotechnol.* **6** 147–50

[3] Zeng H, Dai J, Yao W, Xiao D and Cui X 2012 Valley polarization in MoS$_2$ monolayers by optical pumping *Nat. Nanotechnol.* **7** 490–3

[4] Splendiani A, Sun L, Zhang Y, Li T, Kim J, Chim C Y, Galli G and Wang F 2010 Emerging photoluminescence in monolayer MoS$_2$ *Nano Lett.* **10** 1271–5

[5] Zhao Y *et al* 2013 Interlayer breathing and shear modes in few-trilayer MoS$_2$ and WSe$_2$ *Nano Lett.* **13** 1007–15

[6] Yin Z, Li H, Li H, Jiang L, Shi Y, Sun Y, Lu G, Zhang Q, Chen X and Zhang H 2012 Single-layer MoS$_2$ phototransistors *ACS Nano* **6** 74–80

[7] Novoselov K S, Jiang D, Schedin F, Booth T J, Khotkevich V V, Morozov S V and Geim A K 2005 Two-dimensional atomic crystals *Proc. Natl Acad. Sci. USA* **102** 10451–3

[8] Lee Y-H *et al* 2012 Synthesis of large-area MoS$_2$ atomic layers with chemical vapor deposition *Adv. Mater.* **24** 2320–5

[9] Ling X, Lee Y-H, Lin Y, Fang W, Yu L, Dresselhaus M S and Kong J 2014 Role of the seeding promoter in MoS$_2$ growth by chemical vapor deposition *Nano Lett.* **14** 464–72

[10] Kang K, Xie S, Huang L, Han Y, Huang P Y, Mak K F, Kim C-J, Muller D and Park J 2015 High-mobility three-atom-thick semiconducting films with wafer-scale homogeneity *Nature* **520** 656–60

[11] Hao W, Marichy C and Journet C 2019 Atomic layer deposition of stable 2D materials *2D Mater.* **6** 012001

[12] Pyeon J J, Kim S H, Jeong D S, Baek S H, Kang C Y, Kim J S and Kim S K 2016 Wafer-scale growth of MoS$_2$ thin films by atomic layer deposition *Nanoscale* **4** 6637–41

[13] Song J-G *et al* 2013 Layer-controlled, wafer-scale, and conformal synthesis of tungsten disulfide nanosheets using atomic layer deposition *ACS Nano* **7** 11333–40

[14] Wang X, Feng H, Wu Y and Jiao L 2013 Controlled synthesis of highly crystalline MoS$_2$ flakes by chemical vapor deposition *J. Am. Chem. Soc.* **135** 5304–7

[15] Liu Z *et al* 2014 Strain and structure heterogeneity in MoS$_2$ atomic layers grown by chemical vapour deposition *Nat. Commun.* **5** 5246

[16] Ahn G H, Amani M, Rasool H, Lien D H, Mastandrea J P, Ager J W, Dubey M, Chrzan D C, Minor A M and Javey A 2017 Strain-engineered growth of two-dimensional materials *Nat. Commun.* **8** 608

[17] Raja A *et al* 2017 Coulomb engineering of the bandgap and excitons in two-dimensional materials *Nat. Commun.* **8** 15251

[18] Rösner M, Steinke C, Lorke M, Gies C, Jahnke F and Wehling T O 2016 Two-dimensional heterojunctions from nonlocal manipulations of the interactions *Nano Lett.* **16** 2322–7

[19] Lien D H *et al* 2015 Engineering light outcoupling in 2D materials *Nano Lett.* **15** 1356–61

[20] Chen B, Sahin H, Suslu A, Ding L, Bertoni M I, Peeters F M and Tongay S 2015 Environmental changes in MoTe$_2$ excitonic dynamics by defects-activated molecular interaction *ACS Nano* **9** 5326–32

[21] Liang J, Xu K, Toncini B, Bersch B, Jariwala B, Lin Y C, Robinson J and Fullerton-Shirey S K 2019 Impact of post-lithography polymer residue on the electrical characteristics of MoS$_2$ and WSe$_2$ field effect transistors *Adv. Mater. Interfaces* **6** 1801321

[22] Song J G, Kim S J, Woo W J, Kim Y, Oh I K, Ryu G H, Lee Z, Lim J H, Park J and Kim H 2016 Effect of Al$_2$O$_3$ deposition on performance of top-gated monolayer MoS$_2$-based field effect transistor *ACS Appl. Mater. Interfaces* (https://doi.org/10.1021/acsami.6b07271)

[23] Woo W J *et al* 2018 Bi-layer high-*k* dielectrics of Al$_2$O$_3$/ZrO$_2$ to reduce damage to MoS$_2$ channel layers during atomic layer deposition *2D Mater.* **6** 015019

[24] Zou X *et al* 2014 Interface engineering for high-performance top-gated MoS$_2$ field-effect transistors *Adv. Mater.* **26** 6255–61

[25] Zhang H *et al* 2017 MoS$_2$ functionalization with a sub-Nm thin SiO$_2$ layer for atomic layer deposition of high-κ dielectrics *Chem. Mater.* **29** 6772–80

[26] Kastl C, Chen C T, Kuykendall T, Shevitski B, Darlington T P, Borys N J, Krayev A, Schuck P J, Aloni S and Schwartzberg A M 2017 The important role of water in growth of monolayer transition metal dichalcogenides *2D Mater.* **4** 021024

[27] Lin Y-C, Zhang W, Huang J-K, Liu K-K, Lee Y-H, Liang C-T, Chu C-W and Li L-J 2012 Wafer-scale MoS$_2$ thin layers prepared by MoO$_3$ sulfurization *Nanoscale* **4** 6637

[28] Gutiérrez H R, Perea-López N, Elías A L, Berkdemir A, Wang B, Lv R, López-Urías F, Crespi V H, Terrones H and Terrones M 2013 Extraordinary room-temperature photoluminescence in triangular WS$_2$ monolayers *Nano Lett.* **13** 3447–54

[29] Verre R, Baranov D G, Munkhbat B, Cuadra J, Käll M and Shegai T 2019 Transition metal dichalcogenide nanodisks as high-index dielectric mie nanoresonators *Nat. Nanotechnol.* **14** 679–83

[30] Chen C T *et al* 2019 Very high refractive index transition metal dichalcogenide photonic conformal coatings by conversion of ALD metal oxides *Sci. Rep.* **9** 2768

[31] Nandi D K and Sarkar S K 2014 Atomic layer deposition of tungsten oxide for solar cell application *Energy Procedia* **54** 782–8

[32] McCreary A *et al* 2016 Distinct photoluminescence and raman spectroscopy signatures for identifying highly crystalline WS$_2$ monolayers produced by different growth methods *J. Mater. Res.* **31** 931–44

[33] Berkdemir A *et al* 2013 Identification of individual and few layers of WS$_2$ using Raman spectroscopy *Sci. Rep.* **3** 1755

[34] Cabrini S and Kawata S 2012 *Nanofabrication Handbook* (Boca Raton, FL: CRC Press)

[35] Placidi M *et al* 2015 Multiwavelength excitation Raman scattering analysis of bulk and two-dimensional MoS$_2$: vibrational properties of atomically thin MoS$_2$ layers *2D Mater.* **2** 035006

[36] Nam D, Lee J U and Cheong H 2015 Excitation energy dependent raman spectrum of MoSe$_2$ *Sci. Rep.* **5** 17113

[37] Zhao W, Ghorannevis Z, Amara K K, Pang J R, Toh M, Zhang X, Kloc C, Tan P H and Eda G 2013 Lattice dynamics in mono- and few-layer sheets of WS$_2$ and WSe$_2$ *Nanoscale* **8** 9677

[38] Li H, Lu G, Wang Y, Yin Z, Cong C, He Q, Wang L, Ding F, Yu T and Zhang H 2013 Mechanical exfoliation and characterization of single- and few-layer nanosheets of WSe$_2$, TaS$_2$, and TaSe$_2$ *Small* **9** 1974–81

[39] Durham D B, Ogletree D F and Barnard E S 2018 Scanning Auger spectromicroscopy using the scopefoundry software platform *Surf. Interface Anal.* **50** 1174–9

[40] Hunter J D 2007 Matplotlib: a 2D graphics environment *Comput. Sci. Eng.* **9** 99–104

[41] Jones E and Oliphant E 2001 *SciPy: Open Source Scientific Tools for Python* https://scipy.org/ (Accessed: 21 May 2019)

[42] de la Peña F *et al* 2018 *Hyperspy v1.4.1* (https://doi.org/10.5281/ZENODO.1469364)

[43] Luce R, Hildebrandt P, Kuhlmann U and Liesen J 2016 Using separable nonnegative matrix factorization techniques for the analysis of time-resolved Raman spectra *Appl. Spectrosc.* **70** 1464–75